Hindawi
International Journal of Energy Research
Volume 2023, Article ID 1868528, 21 pages
https://doi.org/10.1155/2023/1868528

WILEY | Hindawi

Research Article

Study on Braking Energy Recovery Control Strategy for Four-Axle Battery Electric Heavy-Duty Trucks

Xuebo Li, Jian Ma, Xuan Zhao, and Lu Wang

School of Automobile, Chang'an University, Xi'an 710064, China

Correspondence should be addressed to Jian Ma; majian@chd.edu.cn and Xuan Zhao; zhaoxuan@chd.edu.cn

Received 1 September 2022; Accepted 29 September 2022; Published 6 February 2023

Academic Editor: Alexey Mikhaylov

Regenerative braking can extend the driving range and reduce PM emissions from abrasion for battery electric heavy-duty trucks (BETs). The composite braking control strategy including torque distribution and dynamic coordinated control for the four-axle BET equipped with the electromechanical braking system is studied. A segmented torque distribution strategy is proposed to maximize energy recovery while ensuring braking stability. The simulation results reveal that the strategy shows better comprehensive braking performance than the two benchmark strategies, and the energy recovery rate in different load states under CHTC-D is above 40%. The proposed coordinated control strategy takes advantage of regenerative braking's rapid response and precise control to compensate for torque deviations caused by the hysteresis of friction braking. For two common braking mode transition conditions, regenerative braking torque correction and advance of the mode switching timing are adopted to enable the motor to obtain the torque compensation ability. This method leads to a slight loss of braking energy, and the maximum torque deviation during the mode switching process is suppressed to less than 1.4 kN·m, and the jerk and braking distance is reduced accordingly, which is of great importance in improving driving comfort and braking safety.

1. Introduction

Heavy-duty trucks (HDTs) have an irreplaceable position in freight transportation. Owing to the large share of fossil fuel consumption and exhaust emissions, regulations and policies have been promulgated by countries to promote HDTs' development towards zero emissions and renewable energy [1, 2]. Battery electric heavy-duty trucks (BETs) have superiority in short-haul transportation [3], and the maturity of battery fast charging technology and the popularization of charging stations are continuously enhancing the competitiveness of BETs in long-haul transportation [4, 5].

Regenerative braking, as a key technology for electric vehicles (EVs), converts the kinetic and potential energy of the vehicle into electrical energy and stores it in the energy storage device to achieve braking energy recovery [6]. The energy consumed during braking accounts for about half of the total driving energy in typical urban driving cycles and is considerable even in expressway driving cycles with low acceleration and deceleration frequency, accounting for 15% [7]. Recycling this braking energy can effectively improve energy utilization efficiency and extend the driving range. Furthermore, regenerative braking plays a vital role in PM_{10} and $PM_{2.5}$ emission reduction for BETs by reducing the use of friction braking [8].

Ample researches have been conducted on electromechanical composite braking control strategies, which are mainly divided into two aspects: braking torque distribution and dynamic coordinated control. The distribution of braking torque between axles mainly affects the braking efficiency and stability and restricts the regenerative braking of the drive axle. Li et al. [9] distributed the braking torque between the front and rear axles based on the ECE regulation curve and ideal braking force distribution curve (I curve). Spichartz and Sourkounis [10] proposed an adaptive distribution method based on real-time road adhesion coefficient estimation. The braking torque is distributed to the drive axle to maximize the recoverable braking energy when the braking intensity is less than the adhesion coefficient. The braking torque is distributed according to the I curve when the braking intensity is larger than the adhesion coefficient, which can make full use of the adhesion conditions

while ensuring vehicle direction stability. Zhang et al. [11] proposed a simplified braking torque distribution method for rear-drive EVs. When the braking intensity exceeds the preset threshold, the rear axle braking torque remains constant, and the front axle braking torque starts to intervene and increase. When the braking intensity increases further, the braking torque of the front and rear axles is distributed in a fixed proportion.

The distribution of regenerative braking and friction braking torque of the drive axle determines the amount of recovered braking energy, which is associated with the energy utilization efficiency of EVs. The rule-based torque distribution strategy is easy to implement and requires only minor modifications to the composite braking system. Kumar and Subramanian [12] improved the conventional parallel torque distribution strategy by adding a linear solenoid actuator between the brake pedal and the brake booster to produce an additional period of idle pedal travel, in which the regenerative braking works alone. The road test results showed that the braking energy recovered by the improved strategy is nearly doubled in an urban driving scenario. Zhang et al. [13] developed three strategies to achieve maximum regeneration efficiency, good pedal feel, and coordination of the former two without changing the original braking torque distribution of the front and rear axles. Xu et al. [14] formulated torque distribution rules based on the identified braking intentions. The braking torque is preferentially provided by the motor under slight and middle braking, while regenerative braking is withdrawn to ensure safety under emergency braking.

The fuzzy logic can imitate human reasoning and decision-making behavior, so it is applied to the construction of models and strategies in various fields [15–17]. Xu et al. [18] took the required braking torque, vehicle speed, battery SOC (state of charge), and temperature as inputs and the regenerative braking torque as output, and the fuzzy rules were developed to take into account battery protection, driving safety, and energy recovery. The experimental results show that the fuzzy logic-based strategy can increase the maximum driving range by 25.7%. To address the braking and battery safety issues, Zhang and Dong [19] proposed a dual-fuzzy-logic-controller-based torque distribution strategy, in which slip coefficient, vehicle speed, and braking requirement were selected as inputs of the braking safety controller and battery SOC and temperature were selected as inputs of the battery safety controller. Similarly, Huang et al. [20] adjusted the regenerative braking ratio according to the battery status and actively controlled the charging current to achieve effective battery thermal management. Such strategies have comparatively strong robustness but rely on practical knowledge and massive experimental data, and the fuzzification of vehicle state information may lead to low control precision and poor dynamic performance [21].

The optimization-based torque distribution strategy has attracted more attention in recent years. Considering the constraints of vehicle configuration, motor torque characteristics, battery charge characteristics, and braking regulations, the objective functions were constructed based on different optimization objectives and braking modes. And then, the exhaustive search method [22], genetic algorithm [23], particle swarm optimization algorithm [24], sequential quadratic programming [25], and multidisciplinary design optimization [26] were used to solve the optimal braking torque distribution online or offline. For the online optimization strategy, the number of control variables was reduced or the objective function and constraints of the optimization model were reasonably adjusted to meet the real-time requirement of the industry control [27]. Nevertheless, real-time control of the offline optimization strategy was implemented by constructing lookup table or approximate models [28]. Besides, the artificial neural network was also used in braking torque distribution due to its advantages in processing fuzzy and random data, but the requirements for the quality and quantity of training data are stringent [29].

Due to the difference in response characteristics between the motor and friction braking system, torque deficit or torque fluctuation may occur in the braking mode transition conditions, so it is necessary to study the dynamic coordinated control strategy. Shang et al. [30] enhanced the control precision and response speed of the composite braking system by combining feedforward and feedback control and used friction braking to compensate for the gap that regenerative braking could not meet the total torque demand. This method improves the system dynamic performance to some extent but does not fundamentally eliminate the response characteristics difference between the two braking subsystems. Kwon et al. [31] used proportional-integral (PI) control to make the motor torque response time controllable and improved the transient characteristics of the composite braking system by controlling the response speed of the motor and hydraulic braking system to be consistent. Xu et al. [14] proposed a torque compensation strategy based on fuzzy PI control, using regenerative braking to compensate for the response lag when the pneumatic braking is involved and using pneumatic braking to compensate for the torque deficit when the regenerative braking is withdrawn, but the torque compensation capacity of the motor and the torque compensation speed of the pneumatic braking system were not considered. He et al. [32] corrected the regenerative braking torque only in accordance with braking intensity to ensure that the motor is capable of compensating the torque deviation, yet the torque compensation capacity of the motor is also closely related to its operating state.

The existing studies on composite braking control strategies have been conducted on two-axle EVs, but few on multiaxle BETs. On the one hand, the torque distribution between axles for multiaxle vehicles is more complex, which is related to the locking sequence of wheels and directly affects the braking stability. On the other hand, the recoverable braking energy of BETs is enormous because they are several times heavier than passenger cars. Moreover, the existing coordinated control strategies mostly exploited the response advantage of motor regenerative braking to compensate for torque deviations, but the torque compensation capacity of the motor has not been well studied. Therefore, the composite braking control of the four-axle BET

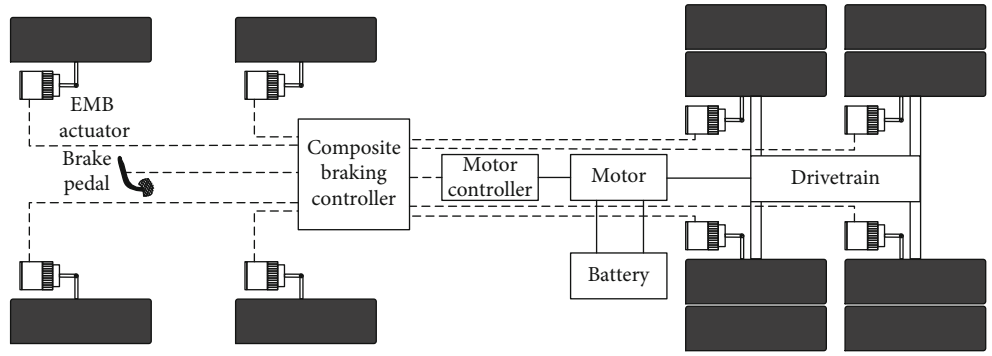

Figure 1: Structure of the composite braking system.

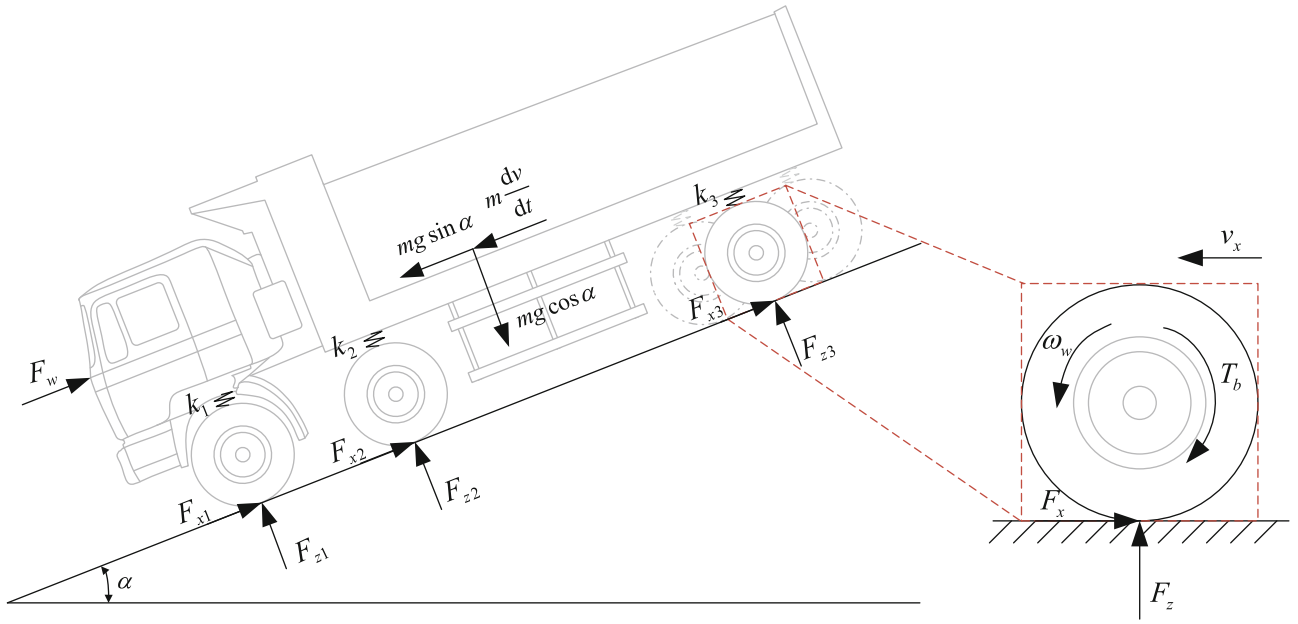

Figure 2: The longitudinal half-vehicle model.

equipped with electromechanical braking (EMB) system is investigated in this paper. A segmented torque distribution strategy is proposed to maximize braking energy recovery while ensuring braking safety, and a coordinated control strategy is proposed to get better dynamic performance for the two common braking mode transition conditions. By analyzing the torque compensation capacity of the motor in the transition condition from regenerative braking to composite braking mode, a fuzzy logic-based correction coefficient is proposed to correct the regenerative braking torque for compensating the torque deviation. In the transition condition from composite braking or regenerative braking to friction braking mode, an EMB intervention trigger speed based on the current braking intensity is proposed to advance the mode switching timing, so that the torque compensation ability can be obtained.

The mass of heavy-duty trucks in unloaded and loaded states varies considerably, which has a great impact on braking performance. For transportation cost considerations, manufacturers usually set the maximum design mass of trucks over the regulation limit, and research has shown that relaxing restrictions on load mass will give further play to the CO_2 reduction for BETs [5, 33]. Therefore, the unloaded, loaded, and overloaded state of the BET should be taken into account in the analysis and simulation.

The remainder of this paper is structured as follows. Section 2 introduces the models of the vehicle, EMB system, and regenerative braking system. The torque distribution strategy and coordinated control strategy are proposed, respectively, in Section 3 and Section 4. Section 5 provides the simulation results and analysis, and the study is summarized in Section 6.

2. Composite Braking System Model

The composite braking system in this study includes two subsystems, the regenerative braking system and the EMB system, which provide regenerative and friction braking torque, respectively. Its structure is shown in Figure 1. The composite braking controller acquires the torque demand

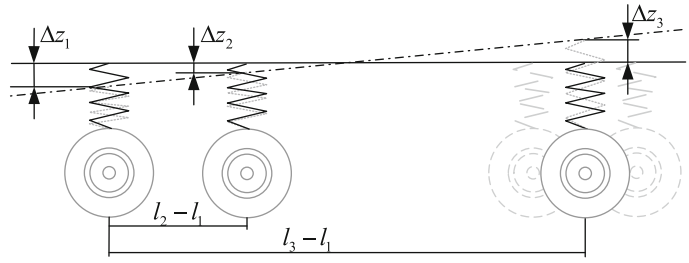

Figure 3: The relationship between suspension deformation.

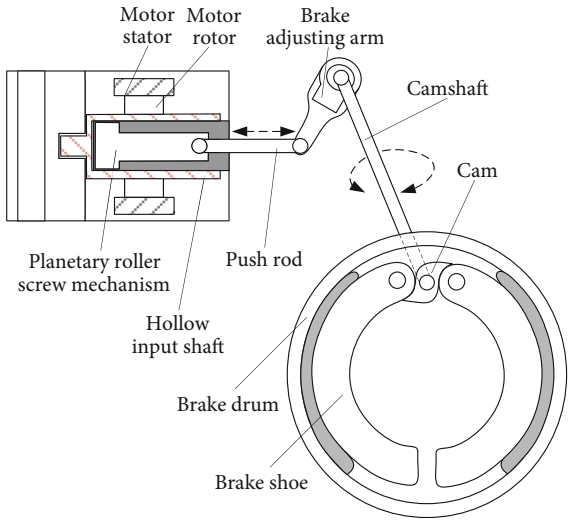

Figure 4: Structure of EMB system.

from the brake pedal signal and distributes the braking torque according to the control strategy and vehicle states and simultaneously sends control commands to the braking subsystems.

2.1. BET Model. This study is aimed at the energy distribution and coordinated control of the four-axle BETs in the braking process, so a longitudinal vehicle dynamic model was developed. The vertical loads on the two rear axles of BETs with tandem suspension are always equal, and the torque from the drivetrain is evenly distributed on both axles, so the two axles are simplified to one axle [34]. Figure 2 shows the forces on the BET during braking, in which the driving resistance is ignored, and the half-vehicle model can be expressed as follows:

$$\begin{cases} m\dfrac{\mathrm{d}v}{\mathrm{d}t} + mg\sin\alpha = -\sum\limits_{i=1,2,3} F_{xi} - \underbrace{\dfrac{C_D A\rho v^2}{2}}_{F_w}, \\ J_{wi}\dfrac{\mathrm{d}\omega_{wi}}{\mathrm{d}t} = \dfrac{R_{wh}F_{xi} - T_{bi}}{2}, \end{cases} \tag{1}$$

where m is the vehicle mass, v is the vehicle speed, g is the acceleration due to gravity, α is the road grade angle, F_{xi} is the ground braking force of the i-axle, F_w is the aerodynamic drag resistance, C_D is the drag coefficient, A is the frontal area, ρ is the air density, J_{wi} is the moment of inertia of the i-axle wheel, ω_{wi} is the wheel speed of the i-axle, R_{wh} is the wheel radius, and T_{bi} is the braking torque of the i -axle, which can be expressed as

$$T_{bi} = \begin{cases} T_{fr}, & i = 1, 2, \\ T_{fr} + T_{reg}, & i = 3, \end{cases} \tag{2}$$

where T_{fr} is the friction braking torque and T_{reg} is the regenerative braking torque.

The ground braking force is the key to vehicle deceleration, so it is necessary to accurately obtain the ground braking force to study the vehicle braking performance. The magic tire model with satisfactory fitting precision and low complexity is adopted, and the expression is as follows [35]:

$$F_{xi} = F_{zi}D_x \sin\{C_x \arctan[B_x s_i - E_x(B_x s_i - \arctan(B_x s_i))]\}, \tag{3}$$

where F_{zi} is the ground normal reaction force of the i-axle, which is equal to the i-axle vertical load, B_x, C_x, D_x, and E_x denote the structural factors related to the tire model, and s_i is the wheel slip ratio, which can be expressed as

$$s_i = 1 - \frac{\omega_{wi}R_{wh}}{v}. \tag{4}$$

The axle load transfer will occur during vehicle braking, and there is a functional relationship between axle load and braking deceleration. According to the forces in the direction perpendicular to the ground in Figure 2, the force and moment equilibrium equations are as follows:

$$\begin{cases} \sum\limits_{i=1}^{3} F_{zi} = mg\cos\alpha, \\ \sum\limits_{i=1}^{3} F_{zi}l_i = mg\cos\alpha l_c - m\left(g\sin\alpha + \dfrac{\mathrm{d}v}{\mathrm{d}t}\right)h_g, \end{cases} \tag{5}$$

where l_i is the distance between the first axle and the i-axle of the BET, l_c is the distance between the first axle and the center of gravity, and h_g is the height of the center of gravity.

To solve the ground normal reaction force of each axle, the suspension constraint is taken into consideration, and the suspension is regarded as an elastic element so that the

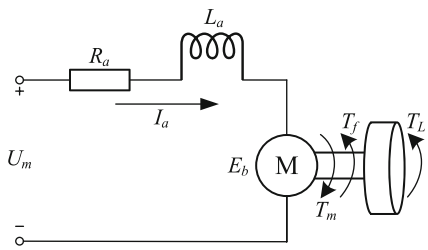

Figure 5: Drive motor equivalent circuit model.

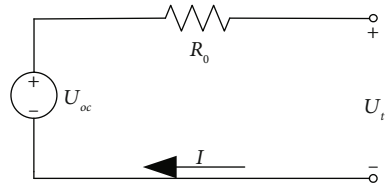

Figure 6: Battery equivalent circuit model.

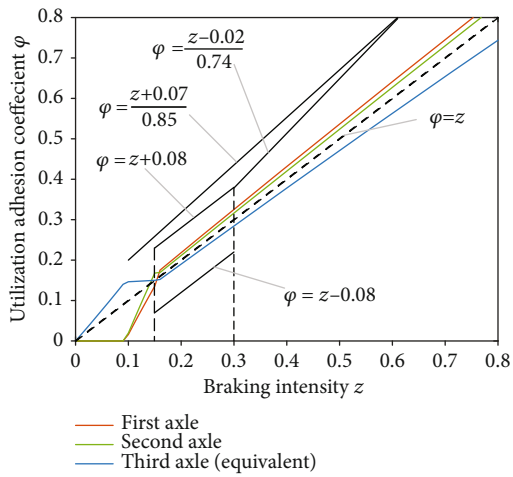

Figure 7: The utilization adhesion coefficient in the loaded state.

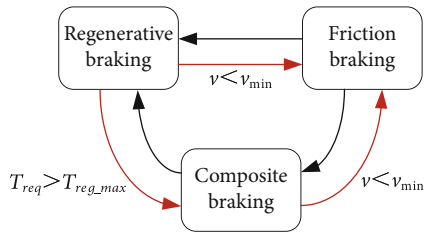

Figure 8: The braking mode transition conditions.

vehicle model is statically determinate. Since the deformation of the frame is much smaller than that of the suspension and tires, the frame is regarded as a rigid body. The deformation relationship of the suspension is simplified, assuming that the connection point between the suspension and the frame is kept in a straight line [36], as shown in Figure 3. In previous studies, the unsprung mass has been usually ignored, or the combined stiffness of suspension and tire has been taken as the overall equivalent stiffness, which may lead to considerable errors. Therefore, the normal reaction force is divided into two parts as follows:

$$F_{zi} = G_i + R_i,\ i = 1, 2, 3, \tag{6}$$

where G_i is the reaction force of the ground to the unsprung mass of the i-axle, and its value is regarded as unchanged during braking, R_i is the reaction force of the frame on the sprung mass of the i-axle, and its value can be obtained from the suspension deformation equation as follows:

$$R_i = k_i \Delta z_i, \quad i = 1, 2, 3, \tag{7}$$

where k_i and Δz_i are the stiffness and the deformation of the i-axle suspension, respectively.

The deformation geometric equation of suspension is obtained from the constraints of frame and suspension as follows:

$$(l_2 - l_1)(\Delta z_3 - \Delta z_1) = (l_3 - l_1)(\Delta z_2 - \Delta z_1). \tag{8}$$

From Equations (6)-(8), the ground normal reaction force of each axle can be solved as follows:

$$\begin{aligned} F_{zi} &= G_i \cos\alpha + K_i\left(g \sin\alpha + \frac{\mathrm{d}v}{\mathrm{d}t}\right) + C_i, \\ K_i &= \frac{mh_g k_i \sum_{j=1}^{3} k_j (l_j - l_i)}{\sum_{j=1}^{3}\sum_{m=1}^{3} k_j k_m (l_2 - l_j)(l_m - l_j)}, \\ C_i &= \frac{mg \cos\alpha k_i \sum_{j=1}^{3} k_j (l_j - l_i)(l_j - l_c)}{\sum_{j=1}^{3}\sum_{m=1}^{3} k_j k_m (l_2 - l_j)(l_m - l_j)}. \end{aligned} \tag{9}$$

2.2. EMB System Model. The EMB system has the advantages of compact structure, high control precision, and good pedal feel, compared with the traditional pneumatic braking system commonly used in HDTs. The decoupling composite braking system, in which the friction braking torque is provided by the EMB system, offers more possibilities for the composite braking control strategy and also supports the hardware basis for the implementation of the strategies.

Different from the disc brake in typical EMB systems, the drum brake is adopted in this study. The structure is shown in Figure 4, and its working principle is as follows: when the driver presses the brake pedal, the composite braking controller identifies the braking intention through the pedal information and sends out the corresponding torque control command. The EMB system controls the drive motor working when received the command, and the rotational motion of the motor is converted into linear motion of the push rod through the planetary roller screw mechanism, which also has the function of reducing speed and generating large torque. The camshaft is driven to rotate by the brake adjusting arm under the thrust from the push rod, and the rotation of the cam causes the brake shoe to push outward and friction with the brake drum to generate braking torque.

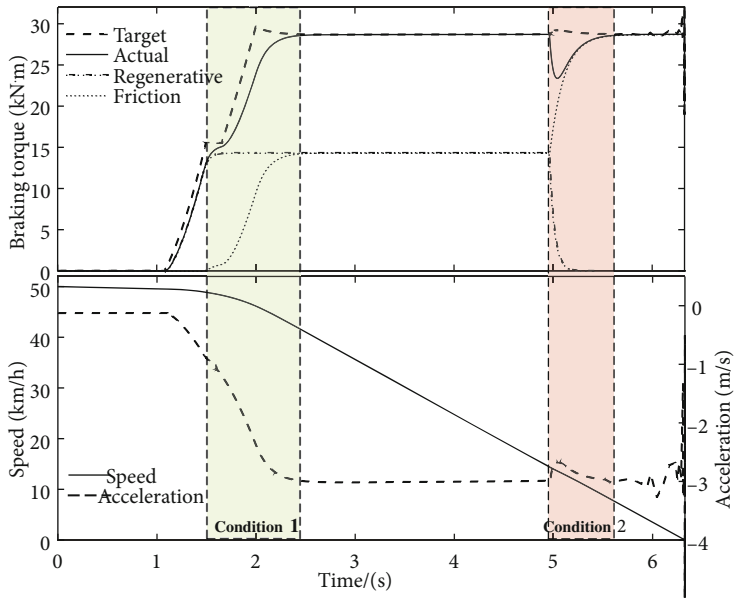

Figure 9: The composite braking process without coordinated control.

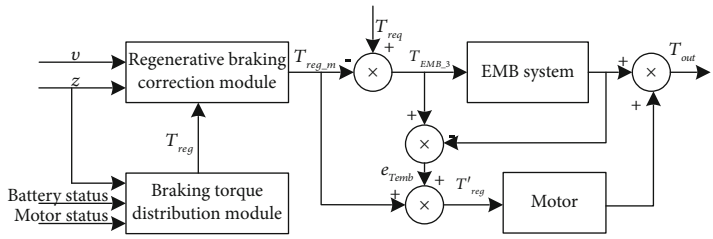

Figure 10: Block diagram of the coordinated controller for transition condition 1.

Table 1: The torque compensation capacity in different load states.

	z (unloaded)				z (loaded)				z (overloaded)			
v	0.3	0.4	0.5	0.6	0.08	0.1	0.2	0.3	0.05	0.1	0.2	0.3
20	100	92.88	89.93	89.93	100	92.71	72	58.22	100	56.96	51.06	37.92
30	100	92.92	85.55	84.79	100	92.71	72.05	58.25	100	57.82	51.25	38
40	100	92.96	85.57	84.82	100	92.71	72.09	58.28	100	59.82	51.28	38.02
50	100	93.01	85.59	84.83	100	92.38	72.24	58.35	100	55.48	51.46	38.44
60	100	89.01	83.42	83.42	91.02	77.09	64.47	53.05	100	40.14	41.26	30.09
70	88.9	80.11	79.64	79.64	75.33	61.62	54.98	43.36	83.14	20.85	22.73	16.19
80	82	76.68	76.72	76.72	62.29	48.4	46.67	34.53	68.66	3.35	4.39	3.66

The permanent magnet DC motor is selected as the drive motor of the EMB system, and its equivalent circuit is shown in Figure 5. The general motor model is constructed as follows:

$$\begin{cases} U_a = L_a \dfrac{\mathrm{d}I_a}{\mathrm{d}t} + R_a I_a + E_b, \\ E_b = K_e \dfrac{\mathrm{d}\theta_m}{\mathrm{d}t}, \\ J_m \dfrac{\mathrm{d}^2\theta_m}{\mathrm{d}t^2} = T_m - T_f - T_L, \\ T_m = K_T I_a, \end{cases} \tag{10}$$

where U_a, L_a, I_a, and R_a are motor armature voltage, inductance, current, and resistance, respectively, E_b is the back electromotive force (EMF), K_e and K_T are the back EMF constant and torque constant, respectively, θ_m is the motor rotation angle, J_m is the moment of inertia of the motor, and T_m, T_f, and T_L are electromagnetic torque, friction torque, and load torque of the motor, respectively.

The planetary roller screw mechanism is selected as the motion conversion mechanism to convert rotational motion into linear motion, which includes planetary carrier and planetary roller set. The planetary roller has external threads to match the internal threads of the hollow input shaft, which is fixedly connected with the motor rotor. The

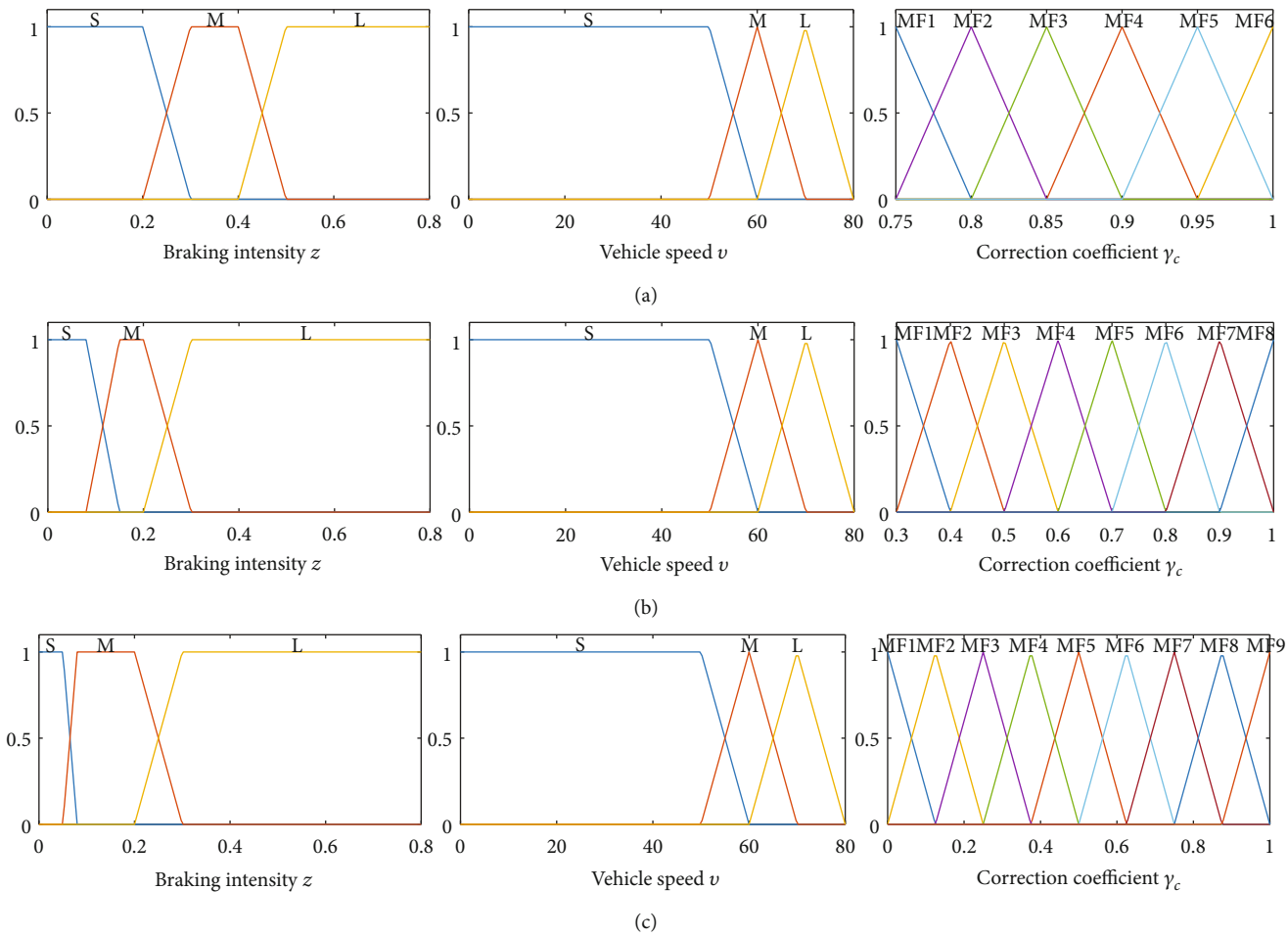

Figure 11: The membership function of input and output in (a) the unloaded state, (b) the loaded state, and (c) the overloaded state.

Table 2: Fuzzy rules base.

	z (unloaded)			z (loaded)			z (overloaded)		
v	S	M	L	S	M	L	S	M	L
S	MF6	MF6	MF5	MF8	MF7	MF6	MF9	MF7	MF6
M	MF4	MF3	MF2	MF5	MF4	MF2	MF5	MF4	MF1
L	MF3	MF2	MF1	MF3	MF3	MF1	MF3	MF2	MF1

displacement of the push rod can be derived as follows:

$$x = \frac{s\theta_m}{2\pi i}, \tag{11}$$

where i is the transmission ratio between the hollow input shaft and the planetary roll and s is the thread lead of the planetary roller.

The linear relationship between displacement and thrust of the push rod has been proven by bench test, so the push rod force can be expressed as follows:

$$F_{pr} = K_{pr}x, \tag{12}$$

where K_{pr} is the thrust coefficient of the push rod.

The torque generated by the thrust reaction of the push rod on the planetary roller is equal to the torque borne by the hollow input shaft, so the load torque of the drive motor can be expressed as follows:

$$T_L = \frac{F_{pr}s}{2\pi\eta}, \tag{13}$$

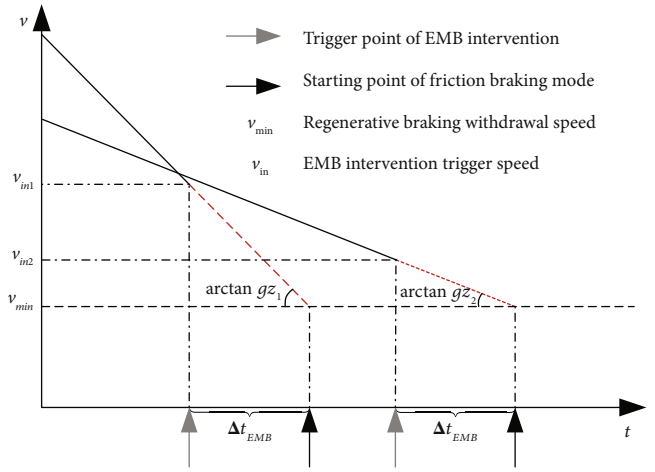

Figure 12: Schematic diagram of EMB intervention trigger speed.

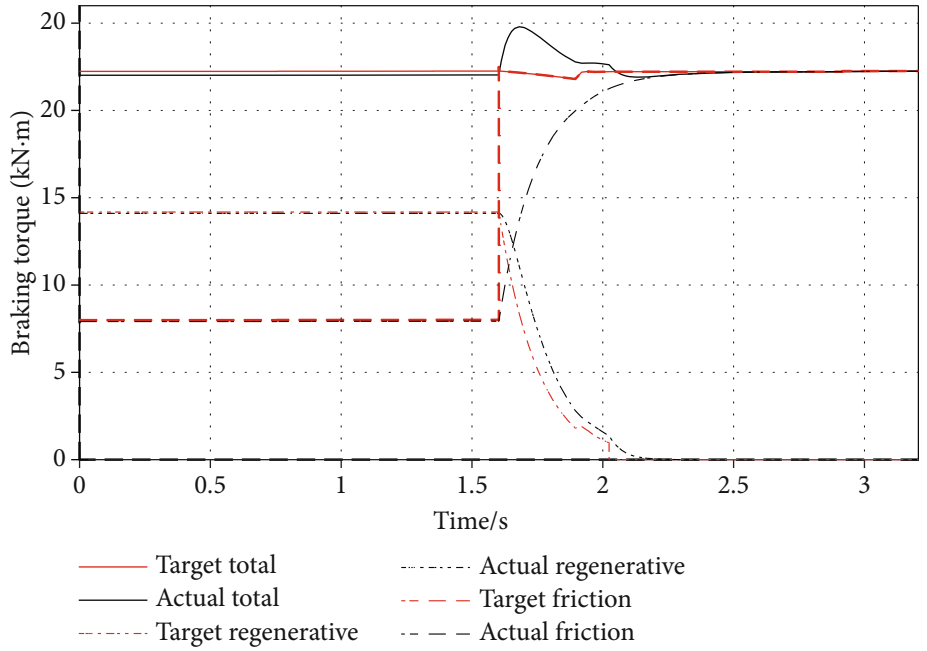

Figure 13: The coordinated control without adjustment factor.

where η is the mechanical efficiency of the motion conversion mechanism.

The cam drum brake is adopted in the EMB system, and its mathematical model of braking torque is described by

$$T_{fr} = K_b \eta_b R_b \frac{L_b}{r_c} F_{pr}, \tag{14}$$

where K_b is the brake efficiency factor, η_b is the mechanical efficiency of the actuating mechanism, R_b is the radius of the brake drum, L_b is the length of the brake adjusting arm, and r_c is the effective radius of the cam.

2.3. Regenerative Braking System Model. The motor, as the core component of the regenerative braking system, works in generator mode during regenerative braking. The kinetic energy of the vehicle is converted into electrical energy and stored in the battery, while braking torque is generated and transmitted to the wheels through the drivetrain.

The motor model is established based on the performance test data, which is obtained through the bench test and stored in the data table, and then, the motor efficiency corresponding to the torque and rotation speed is obtained by using the lookup tables. The maximum regenerative braking torque of the motor can be expressed as follows:

$$T_m = \begin{cases} T_{m\_\max} \eta_m, & n \le n_b, \\ \dfrac{9550 P_{m\_\max} \eta_m}{n}, & n > n_b, \end{cases} \tag{15}$$

Table 3: Main parameters of the BET.

Item	Parameter	Value
Vehicle	Mass (kg)	45000 (overloaded)/31000(loaded)/14500 (unloaded)
	Wheelbase (m)	1.8 + 3.2 + 1.4
	Height of the center of gravity (m)	1.8 (overloaded and loaded)/1.4 (unloaded)
	Distance between the first axle and the center of gravity (m)	4.1 (overloaded and loaded)/3.4 (unloaded)
Transmission	Gear ratio	6.5/4.0/2.1/1
Main reducer	Gear ratio	5.7
Motor	Maximum torque (N·m)	2500
	Maximum power (kW)	360
Battery	Capacity (A·h)	645
	Nominal voltage (V)	615

where $T_{m\_\max}$ is the maximum torque of the motor, $P_{m\_\max}$ is the maximum power of the motor, η_m is the motor efficiency, and n and n_b are motor rotation speed and the rated speed, respectively.

To well reflect the dynamic characteristics of the motor, the torque response is regarded as a first-order inertia link:

$$T_{m\_\text{act}} = \frac{1}{\tau_m s + 1} T_{m\_\text{ref}}, \tag{16}$$

where T_{m_act} and T_{m_ref} are the actual torque and target torque of the motor, respectively, and τ_m is the time constant of the motor.

As the energy storage device of BETs, batteries are used to store the recovered braking energy during regenerative braking. Battery models are mainly divided into three categories: electrochemical model, mathematical model, and equivalent circuit model [37]. In this study, the Rint equivalent circuit model is used to estimate the battery state, which includes an ideal voltage source and an equivalent resistance, as shown in Figure 6. Based on Kirchhoff's law and the relationship between battery power, voltage, and current, it yields

$$\begin{cases} I = \dfrac{U_{oc} - \sqrt{{U_{oc}}^2 - 4R_0 P_{bat}}}{2R_0}, \\ U_t = \dfrac{P_{bat}}{I}, \end{cases} \tag{17}$$

where P_{bat} is the battery charging power, U_t and I are the battery output voltage and current, respectively, and U_{oc} and R_0 are the open circuit voltage and the internal resistance, respectively.

Battery SOC is obtained by ampere-hour integral method:

$$\text{SOC}(t) = \text{SOC}(t_0) - \frac{1}{C_n}\int_{t_0}^{t} I(t)\mathrm{d}t, \tag{18}$$

where $\text{SOC}(t)$ is the battery SOC at time t, $\text{SOC}(t_0)$ is the initial SOC, and C_n is the battery capacity.

The regenerative braking torque from the motor is transmitted to the wheel through the transmission, drive shaft, and main reducer. Automated mechanical transmission (AMT) is widely adopted in HDTs for its high efficiency and low cost. Considering that the dynamic characteristics of AMT have little impact on vehicle braking, the shift actuator is ignored [38], and the simplified AMT model can be expressed as

Table 4: Optimized braking force distribution coefficient.

Load state	Braking force distribution coefficient		
	β_1	β_2	β_3
Unloaded	0.3	0.23	0.47
Loaded	0.28	0.22	0.5
Overloaded	0.29	0.22	0.49

$$\begin{cases} T_{tr} = T_{mot} i_g \eta_{tr} - J_{tr}\dfrac{\mathrm{d}n_{tr}}{\mathrm{d}t}, \\ n_{tr} = \dfrac{n_{mot}}{i_g}, \end{cases} \tag{19}$$

where T_{tr} and T_{mot} are AMT output and input torque, respectively, i_g is the gear ratio of AMT, η_{tr} is transmission efficiency, J_{tr} is the moment of inertia of AMT output shaft, and n_{tr} and n_{mot} are AMT output and input rotation speed, respectively.

Similarly, the model of the drive shaft and main reducer can be expressed as

$$\begin{cases} T_{fd} = T_{tr} i_0 \eta_{sh} \eta_{fd} - J_{sh}\dfrac{\mathrm{d}n_{sh}}{\mathrm{d}t} - J_{fd}\dfrac{\mathrm{d}n_{fd}}{\mathrm{d}t}, \\ n_{sh} = n_{tr},\ n_{fd} = \dfrac{n_{sh}}{i_0}, \end{cases} \tag{20}$$

where T_{fd} is the output torque of the main reducer, i_0 is the gear ratio of the main reducer, η_{sh} and η_{fd} are the transmission efficiency of the drive shaft and the main reducer, respectively, J_{sh} and J_{fd} are the moment of inertia of the drive shaft and the main reducer, respectively, and n_{sh} and n_{fd} are the rotation speed of the drive shaft and the output rotation speed of the main reducer, respectively.

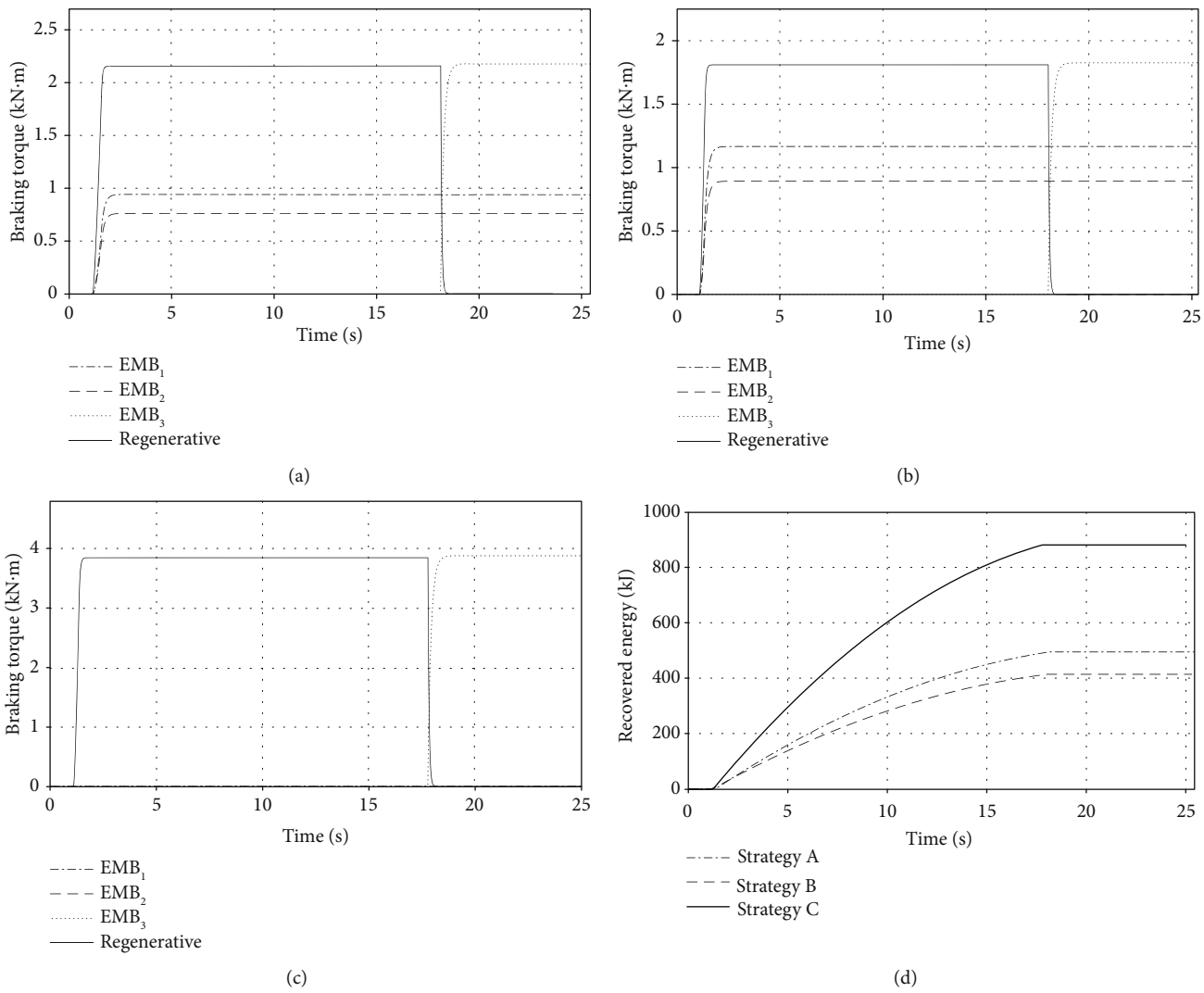

Figure 14: Simulation results in the unloaded state under single braking condition 1. Torque distribution of (a) strategy A, (b) strategy B, and (c) strategy C. (d) Comparison of the recovered energy.

3. The Braking Torque Distribution Strategy

The proposed torque distribution strategy first distributes the braking torque between axles and then distributes the friction braking and regenerative braking torque of the drive axle (the equivalent rear axle in this paper). Whether the torque distribution between axles is reasonable or not directly determines the braking safety of HDTs, and ECE braking regulations stipulate the braking torque distribution between axles of multiaxle vehicles, which can be described as

$$\begin{cases} \varphi_i \le \dfrac{z + 0.07}{0.85}, & 0.1 \le z \le 0.61, \\ z - 0.08 < \varphi_i < z + 0.08, & 0.15 \le z \le 0.3, \\ \varphi_{fi} > \varphi_{ri}, & 0.15 \le z \le 0.3 \\ \varphi_{ri} \le \dfrac{z - 0.02}{0.74}, & z \ge 0.3, \end{cases} \tag{21}$$

where z is the braking intensity, φ_i is the utilization adhesion coefficient of the i-axle, and φ_{fi} and φ_{ri} are the utilization adhesion coefficient of the front and rear axles, respectively.

For BETs, the torque distribution between axles also affects the braking energy recovery; that is, more torque distributed to the drive axle helps to reach the full potential of regenerative braking. A segmented braking torque distribution strategy is developed, and the principle followed is to fully utilize braking energy recovery (distribute as much torque as possible to the equivalent rear axle) while ensuring braking stability and braking efficiency (satisfying ECE regulations). The specific torque distribution strategy is as follows.

If $z < z_0$, then $\beta_1 = \beta_2 = 0$, and $\beta_3 = 1$. The braking torque is distributed to the equivalent rear axle.

If $z_0 < z < 0.15$, then $\beta_3 = 0.15F_{z3}|_{z=0.15}/F_x$, and $\beta_1 = \beta_2 = (1 - \beta_3)/2$. The braking torque of the equivalent rear axle remains constant, and the braking torque of the first and

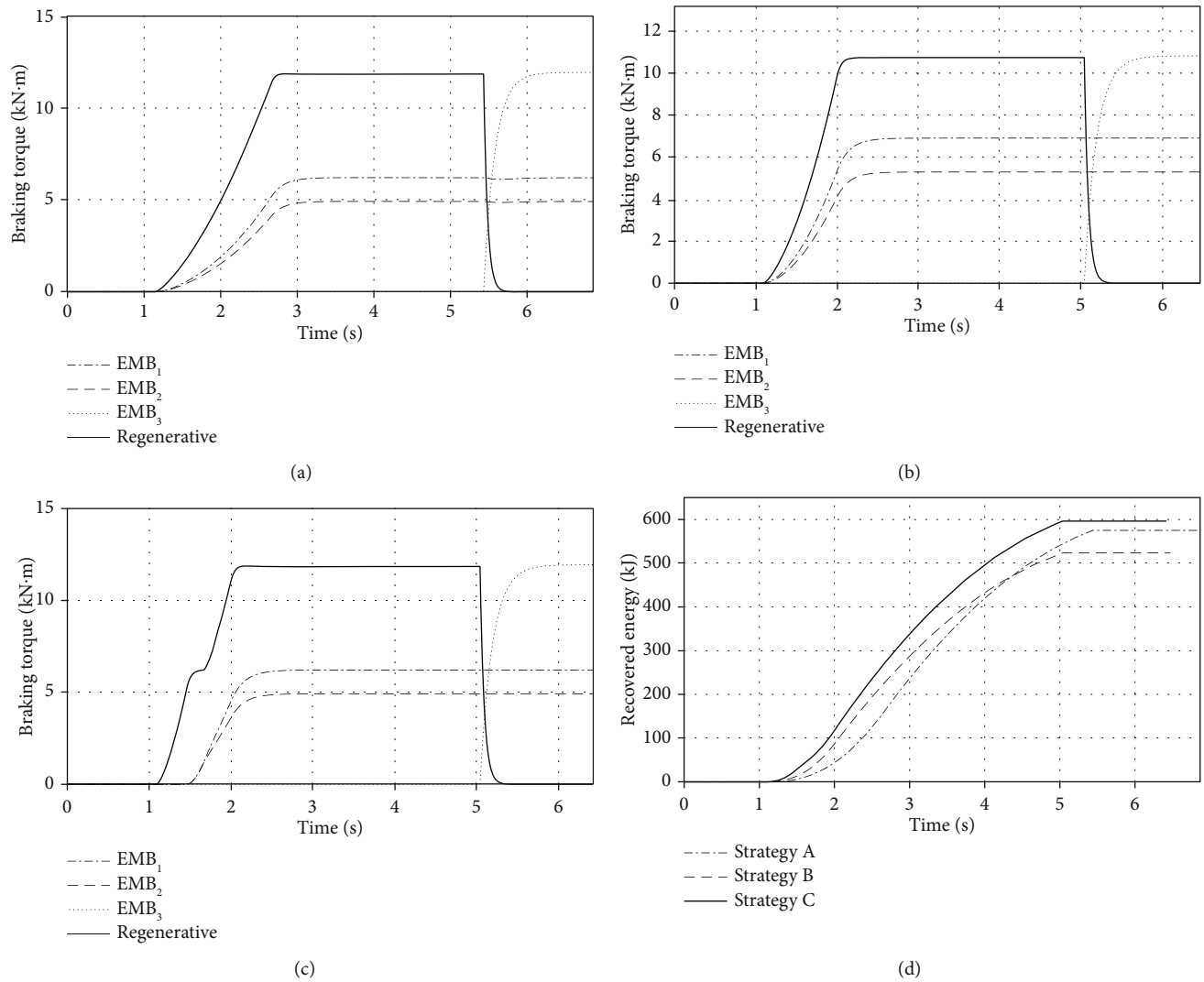

Figure 15: Simulation results in the unloaded state under single braking condition 2. Torque distribution of (a) strategy A, (b) strategy B, and (c) strategy C. (d) Comparison of the recovered energy.

second axles is equally distributed. z_0 is a dynamic threshold, which is determined by the condition

$$\begin{cases} F_x\big|_{z=z_0} \le 0.15 F_{z3}\big|_{z=0.15}, \\ F_x\big|_{z=z_0+0.01} > 0.15 F_{z3}\big|_{z=0.15}, \end{cases} \tag{22}$$

so as to avoid the reduction of equivalent rear axle torque with the increase of braking intensity.

If $z \ge 0.15$, then $\beta_1 = (zF_{z1}/F_x) + 0.02$, $\beta_2 = (zF_{z2}/F_x) + 0.01$, and $\beta_3 = 1 - \beta_1 - \beta_2$. The braking torque is distributed according to a modified optimal braking efficiency strategy. The so-called optimal braking efficiency strategy is to meet the requirement that the utilization adhesion coefficient is equal to the braking intensity, but the braking instability with the rear axle locked first may occur in this case due to the influence of uncertainties such as sensor signal noise or torque control error. Therefore, the strategy is modified to obtain a relatively high braking efficiency while ensuring that the utilization adhesion coefficient of the equivalent rear axle is less than that of the first and second axles at any time. Taking the loaded state as an example, the utilization adhesion coefficient of each axle is shown in Figure 7.

To maximize braking energy recovery, the torque distribution of the drive axle adopts the principle of regenerative braking priority; that is, friction braking only works when regenerative braking cannot meet the torque demand. The torque distribution of the equivalent rear axle is as follows:

$$\begin{cases} T_{reg} = \min\left(T_{req}, T_{\text{reg\_max}}\right), \\ T_{EMB\_3} = T_{req} - T_{reg}, \end{cases} \tag{23}$$

where T_{req} is the required braking torque of the equivalent rear axle, $T_{\text{reg\_max}}$ is the maximum regenerative braking torque, which is related to motor maximum torque, battery SOC and maximum charging power, and T_{EMB_3} is the friction braking torque of the equivalent rear axle.

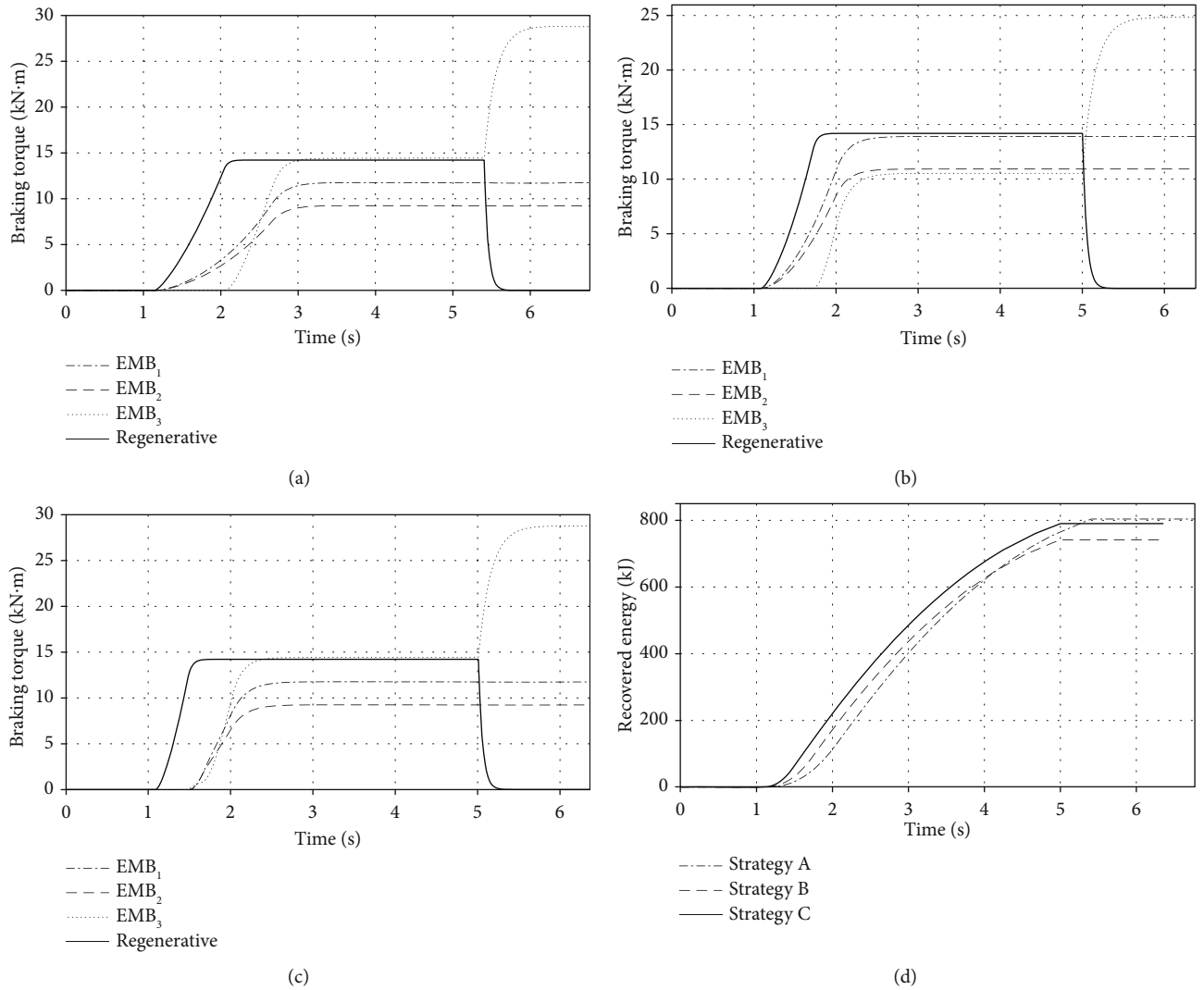

Figure 16: Simulation results in the loaded state under single braking condition 2. Torque distribution of (a) strategy A, (b) strategy B, and (c) strategy C. (d) Comparison of the recovered energy.

Table 5: Simulation results under single braking conditions.

Load state	Torque distribution strategy	Braking time (s)		Braking distance (m)		Recovered energy (kJ)		Energy recovery rate (%)	
		1	2	1	2	1	2	1	2
Unloaded	Strategy A	25.42	6.86	180.5	60.94	495.2	575	35.73	41.5
	Strategy B	25.30	6.46	178.8	55.76	414.2	523.8	29.89	37.8
	Strategy C	25.01	6.41	176.7	55.50	884.4	596.4	63.82	43.04
Loaded	Strategy A	25.20	6.77	180.6	60.69	1273	803.9	42.56	26.89
	Strategy B	25.14	6.38	179.1	55.47	974	741.3	32.58	24.79
	Strategy C	25.01	6.36	178.2	55.38	1952	790.3	65.28	26.43
Overloaded	Strategy A	25.36	6.76	181.4	60.73	1859	846.5	42.83	19.5
	Strategy B	25.13	6.36	179.3	55.43	1398	769.3	32.20	17.73
	Strategy C	25.03	6.36	178.8	55.37	2838	808.4	65.38	18.63

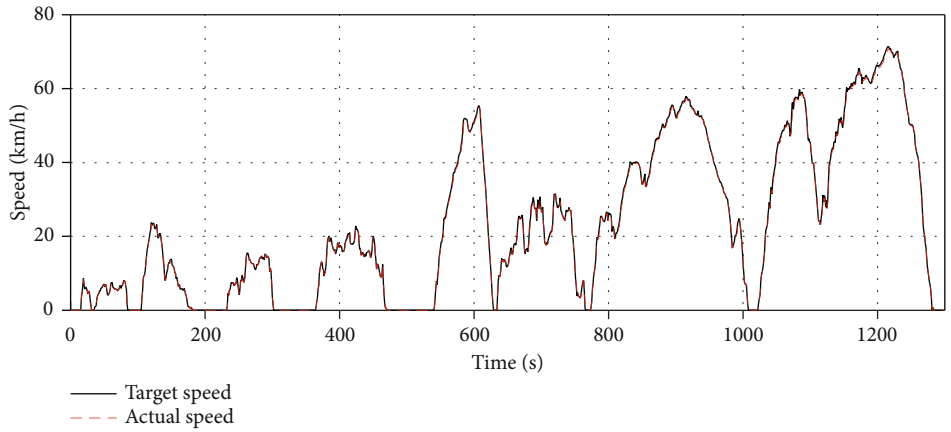

Figure 17: CHTC-D speed following curve.

4. The Dynamic Coordinated Control Strategy

The composite braking system has three braking modes: regenerative braking, friction braking, and composite braking. As driving cycles and vehicle status change, there are two common braking mode transition conditions, as shown in Figure 8.

Transition condition 1: transition from regenerative braking mode to composite braking mode when the torque demand increases and regenerative braking cannot be met

Transition condition 2: transition from composite braking mode (high braking intensity) or regenerative braking mode (low braking intensity) to friction braking mode when the vehicle speed is reduced so that the motor cannot provide regenerative braking torque

Due to the inherent difference in dynamic response characteristics between the motor and the EMB system, response lag and sudden acceleration change will occur during the braking mode switching process. This may not only worsen the riding comfort but also lead to the inconsistent braking feeling, which will affect the driver's judgment and cause misoperation, seriously threatening driving safety.

Figure 9 shows the composite braking process without coordinated control. As the torque demand increases, friction braking begins to participate when regenerative braking torque reaches the maximum and cannot meet the demand. There is a noticeable lag in transition condition 1 due to the relatively slow response of the EMB system. In addition, when the vehicle speed is reduced to about 14 km/h, the motor rotation speed is so low that the back EMF is less than the battery charging voltage, so it is unable to generate regenerative braking torque. At this time, the regenerative braking exits, and the friction braking works independently. Also limited by the response speed of the EMB system, the friction braking cannot compensate for the lack of regenerative braking torque immediately. There is a large difference between the actual torque and the target torque in transition condition 2, which leads to a sudden change of acceleration.

Compared with the EMB system, the motor is superior in aspects of response speed and control precision, so it is feasible to use regenerative braking to compensate for the torque deficit caused by the hysteresis of friction braking. However, in the above two braking mode transition conditions, the motor loses its torque compensation ability because the regenerative braking torque has reached the upper limit or cannot be generated. Consequently, the core of the coordinated control strategy is to enable the motor to obtain the regenerative braking torque compensation ability.

4.1. The Coordinated Control Strategy for Transition Condition 1. During the transition condition 1, the motor regenerative braking torque has reached the maximum, so it is unable to provide additional torque. To obtain the torque compensation ability of the motor and reduce the loss of braking energy recovery simultaneously, the regenerative braking torque is corrected as follows:

$$T_{reg\_m} = \gamma_c T_{reg}, \tag{24}$$

where T_{reg_m} is the corrected regenerative braking torque and γ_c is the correction coefficient with a range of [0, 1], which is related to vehicle speed and braking intensity, and can be expressed as

$$\gamma_c = \begin{cases} \gamma(v, z), & \dot{z} > 0, \\ 1, & \dot{z} \le 0, \end{cases} \tag{25}$$

where $\dot{z}$ is the change rate of braking intensity. The regenerative braking torque is corrected only during the increase of braking intensity, and the original torque distribution strategy is implemented when the braking intensity decreases or remains constant.

The correction of the regenerative braking torque is equivalent to redistributing the braking torques on the drive axle on the basis of the original torque distribution strategy, as shown in Figure 10. The output torque of the composite braking system is as follows:

$$\begin{cases} T_{\mathrm{EMB\_3}} = T_{\mathrm{req}} - T_{\mathrm{reg\_m}}, \\ T'_{\mathrm{reg}} = T_{\mathrm{reg\_m}} + e_{\mathrm{Temb}}. \end{cases} \tag{26}$$

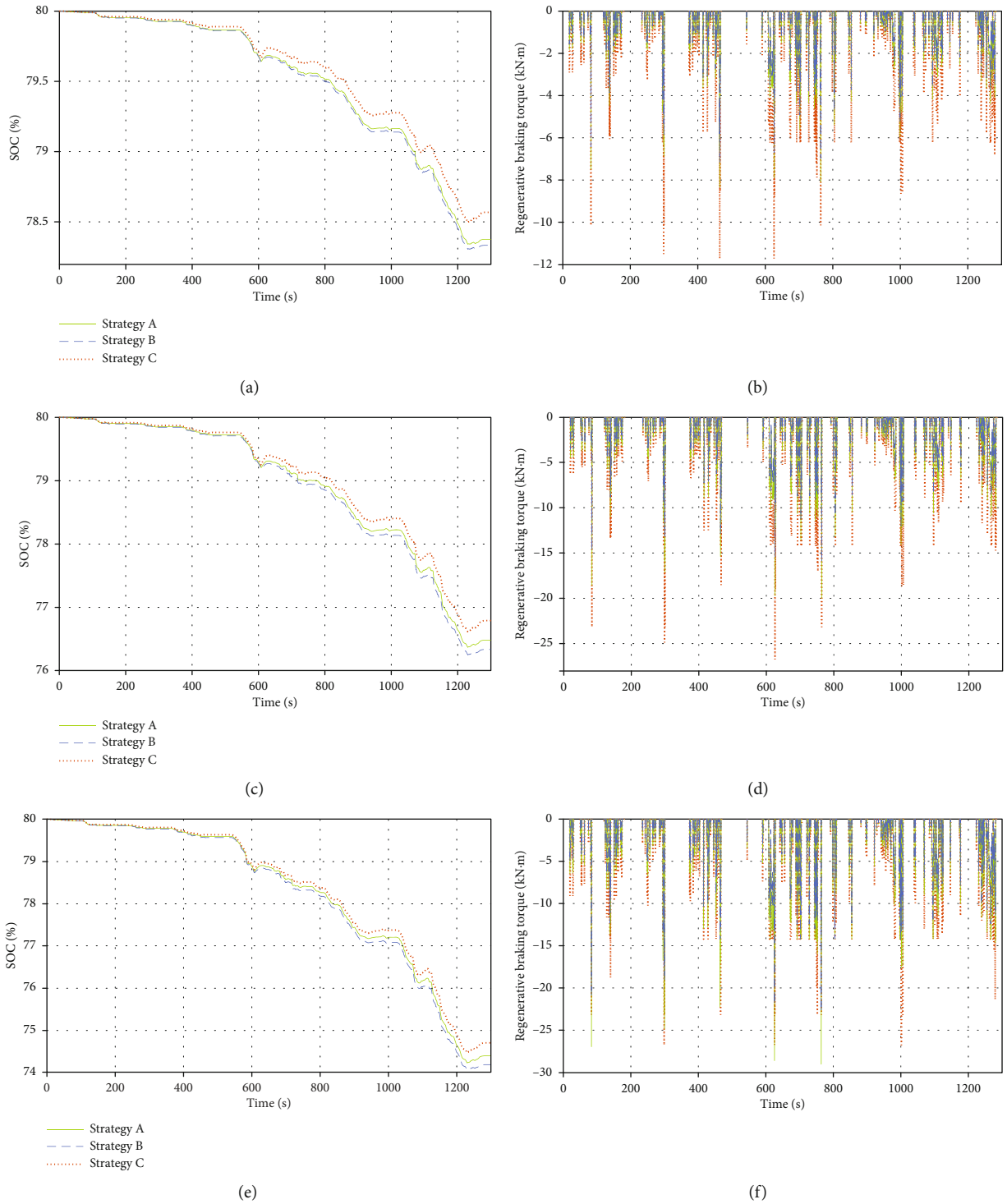

FIGURE 18: Simulation results under CHTC-D condition. Battery SOC in (a) the unloaded state, (c) the loaded state, and (e) the overloaded state. Regenerative braking torque on the equivalent rear axle in (b) the unloaded state, (d) the loaded state, and (f) the overloaded state.

The friction braking torque deviation e_{Temb} (that is, the difference between target torque and actual torque of the EMB system) varies with braking intensity, and the maximum regenerative braking torque is closely related to the motor rotation speed. The shift control during braking is not considered in this study, so there is a fixed relationship between the motor rotation speed and the vehicle speed. Therefore, the torque compensation capacity of the motor, which is defined as $1 - e_{\text{Temb}}/T_{\text{reg\_max}}$, under different braking intensities and vehicle speeds is analyzed, and the results are shown in Table 1. If the value is larger, the motor has a better ability to compensate for the friction braking torque deviation, and the less regenerative braking torque is discarded when it is corrected.

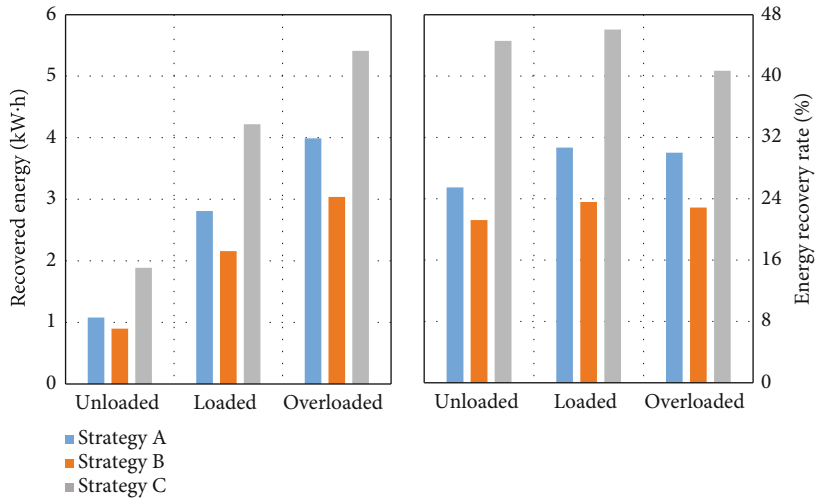

Figure 19: Performance comparison under CHTC-D condition.

It can be seen from the table that the torque compensation capacity of the motor is the largest in the unloaded state and decreases with the increasing load mass of the BET. That is because the torque demand of the drive axle increases with the load mass at the same braking intensity, which will lead to the increase of friction braking torque deviation. The regenerative braking can meet the torque demand of the drive axle at low braking intensity, so there is no need for the motor to compensate for the torque deviation. The torque demand of friction braking increases with the braking intensity, and its torque deviation increases first and then remains at a certain level. The maximum regenerative braking torque is basically constant when the motor rotation speed is less than the rated speed, so the torque compensation capacity is close when the vehicle speed is lower than 50 km/h. With the further increase in vehicle speed, the maximum regenerative braking torque decreases, which will cause the attenuation of the torque compensation capacity.

Based on the above analysis, the regenerative braking torque is corrected by using fuzzy logic. Mamdani-type fuzzy inference model is adopted, with vehicle speed v and braking intensity z as inputs and regenerative braking torque correction coefficient γ_c as output. The membership functions are shown in Figure 11, and the fuzzy rules formulated are shown in Table 2.

4.2. The Coordinated Control Strategy for Transition Condition 2. When the rotation speed drops below the threshold, the back EMF provided by the motor is not enough to charge the battery. In this case, the braking energy cannot be effectively recovered and may cause the problem of motor heating, so the regenerative braking should be withdrawn. The low-speed threshold is dynamic, which is related to the motor specification, battery state, and vehicle driving conditions [39]. Since its influence on the coordinated control research is minimal, a fixed low-speed threshold is set in this study; that is, the regenerative braking is withdrawn when the motor rotation speed is lower than 300 rpm.

With the withdrawal of regenerative braking, composite braking or regenerative braking is transitioned to friction braking mode, and the response lag of the EMB system in the process of filling in the missing regenerative braking will cause a deficit of total braking torque. To complete the compensation of friction braking hysteresis before the regenerative braking withdrawal and eliminate torque deficit, it is necessary to advance the timing of braking mode switching. However, too much advance will lead to a waste of braking energy and reduce the energy recovery efficiency, while not enough advance will not allow the motor to obtain sufficient torque compensation capacity. Therefore, an EMB intervention trigger speed based on the real-time braking intensity was proposed, which controls the EMB system to take over the braking demand in advance, so that the braking mode switching can be completed before the vehicle speed drops to the low-speed threshold, and the impact on the braking energy recovery can be minimized.

Table 6: Parameters of single braking conditions.

Single braking condition	Condition 3	Condition 4	Condition 5
Initial speed (km/h)	30	50	65
Braking intensity	0.05	0.25	0.5

The vehicle speed when regenerative braking is withdrawn can be obtained according to the current vehicle state:

$$v_{\min} = 0.377 \frac{R_{wh} n_{ls}}{i_g i_0}, \tag{27}$$

where n_{ls} is the low-speed threshold of the motor.

As shown in Figure 12, combined with the real-time braking intensity, the EMB intervention trigger speed can be calculated as follows:

$$v_{\text{in}} = v_{\min} + gz\Delta t_{EMB}, \tag{28}$$

where Δt_{EMB} is the response time of the EMB system.

During the braking process, when the vehicle speed drops to the trigger speed, the total torque demand of the drive axle is met by the EMB system, and regenerative

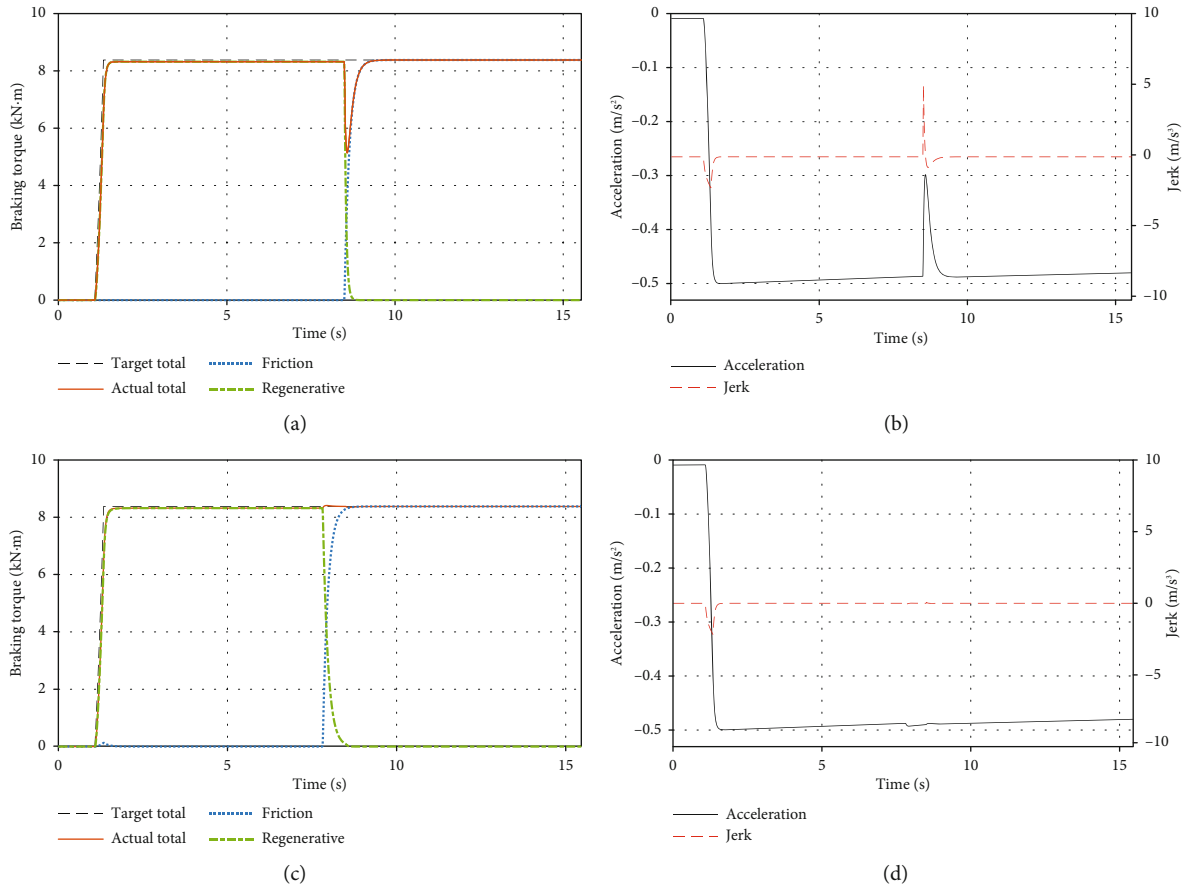

FIGURE 20: Simulation results under single braking condition 3. (a) Braking torque, and (b) acceleration and jerk without coordinated control. (c) Braking torque and (d) acceleration and jerk with coordinated control.

braking is only used to compensate for the friction braking torque deviation. Due to the small hysteresis of motor regenerative braking, the actual total torque is obviously larger than the target torque in the compensation control process, as shown in Figure 13. Therefore, an adjustment factor is introduced to eliminate the inevitable torque deviation caused by the difference in response characteristics when the two braking torques change in reverse (one increases and the other decreases). The output torque of the composite braking system is as follows:

$$\begin{cases} T_{EMB\_3} = T_{req}, \\ T_{reg} = \varsigma_r e_{Temb}, \end{cases} \tag{29}$$

where ς_r is the adjustment factor, which is related to the response characteristics of the motor and the EMB system, and can be taken as 0.6~0.8 by experimental analysis.

5. Simulation Results and Analysis

To verify the effect of the proposed control strategy, the models and control strategy were established in Matlab/Simulink environment. The main parameters of the BET are shown in Table 3.

5.1. Simulation and Analysis of Torque Distribution Strategy. The other two torque distribution strategies were proposed as a comparison, and the simulation tests of single braking conditions and CHTC-D condition were carried out to prove the superiority of the proposed torque distribution strategy in braking energy recovery.

5.1.1. The Benchmark Strategy A (Optimal Braking Efficiency Strategy). When the utilization adhesion coefficient is equal to the braking intensity, the braking efficiency of each axle is optimal in any load state, and the braking force of each axle is as follows:

$$F_{xi} = zF_{zi}. \tag{30}$$

5.1.2. The Benchmark Strategy B (Optimal Fixed Proportion Distribution Strategy). At present, HDTs mostly adopt the fixed proportion distribution strategy, and the braking force distribution coefficient in different load states is adjusted by a load sensing proportioning valve. To meet the requirements of braking stability and make full use of the tire-road adhesion conditions, the distribution coefficient in different load states was optimized. The objective function is to minimize the square sum of the difference between the utilization adhesion coefficient of each axle and the braking

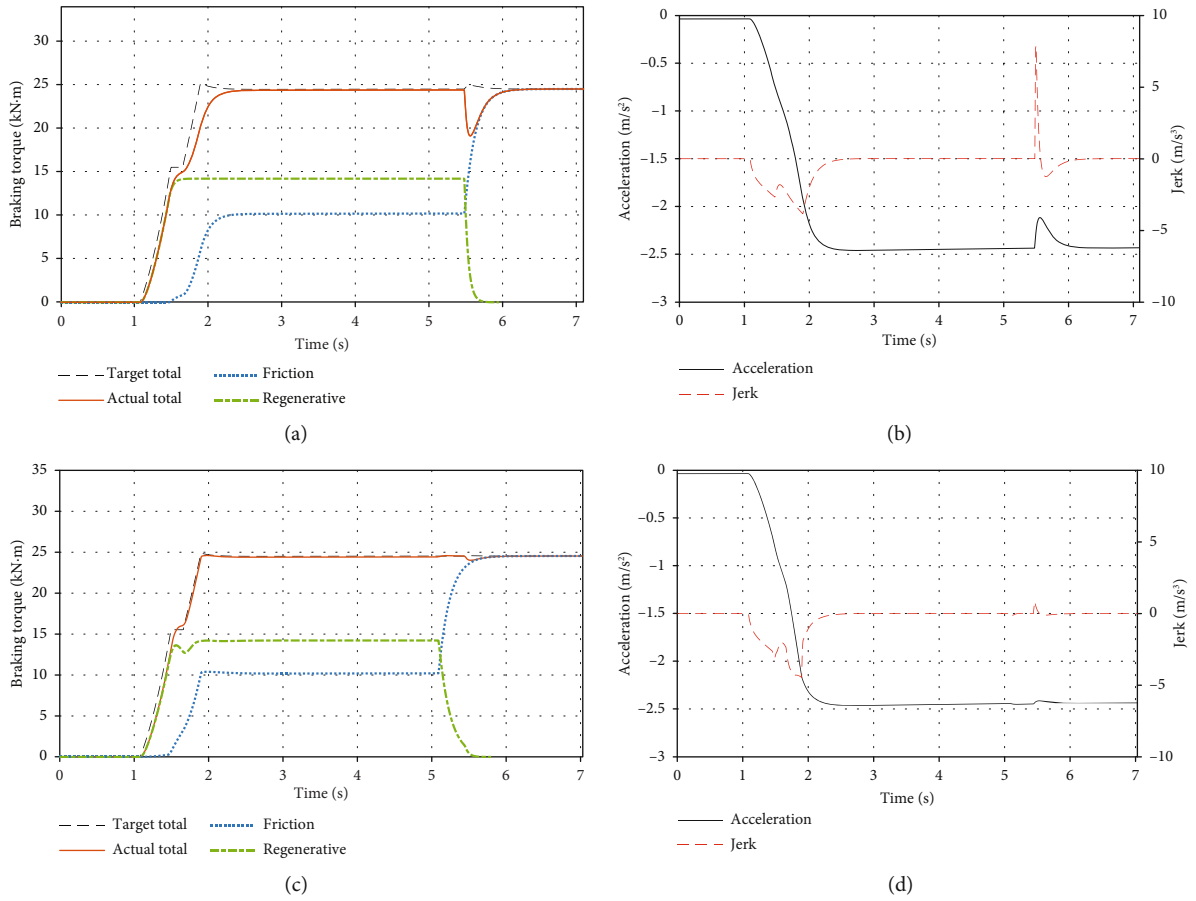

FIGURE 21: Simulation results under single braking condition 4. (a) Braking torque and (b) acceleration and jerk without coordinated control. (c) Braking torque and (d) acceleration and jerk with coordinated control.

intensity, that is,

$$\min \sum_{z=0.01}^{0.8} \sum_{i} (\varphi_i(\beta_i) - z)^2, \tag{31}$$

where utilization adhesion coefficient φ_i is a function of braking force distribution coefficient β_i, which can be expressed as $\varphi_i = \beta_i F_x / F_{zi}$.

The constraint condition is the inequality (21), and the exhaustive search method was used to solve the optimal braking force distribution coefficient in unloaded, loaded, and overloaded states, as shown in Table 4.

5.1.3. Single Braking Condition. To clearly show the torque distribution during braking and its impact on energy recovery, two single braking conditions are set: the initial vehicle speed is 50 km/h, and when the time reaches 1 s, the braking intensity gradually increases to 0.05 (single braking condition 1) and 0.3 (single braking condition 2) and remains constant until the speed decreases to 0. The three torque distribution strategies in different load states were simulated and compared. It should be noted that strategy A refers to the optimal braking efficiency strategy, strategy B refers to the optimal fixed proportion distribution strategy, and strategy C refers to the proposed segmented distribution strategy.

Taking the unloaded state as an example, the comparison of torque distribution and recovered energy under two single braking conditions is shown in Figures 14 and 15. The braking intensity of single braking condition 1 is small, and part of the braking torque is assigned to the front two axles in strategy A and strategy B, while the braking torque is all provided by the equivalent rear axle in strategy C. The regenerative braking torque can meet the torque demand, so the EMB system of the rear axle only works after the regenerative braking is withdrawn. As the proportion of regenerative braking increases, more braking energy is recovered. Figure 14(d) shows that strategy C has a huge advantage in braking energy recovery at low braking intensity.

Under single braking condition 2, the EMB systems of the front two axles participate in the whole braking process in strategy A and strategy B, while they gradually start to work as the braking intensity increases in strategy C.

With the increase of the load mass or braking intensity, the energy recovery capacity of strategy C is slightly inferior to that of strategy A. Figure 16 shows the simulation results in the loaded state under single braking condition 2, and more braking energy is recovered in strategy A because of its long braking time.

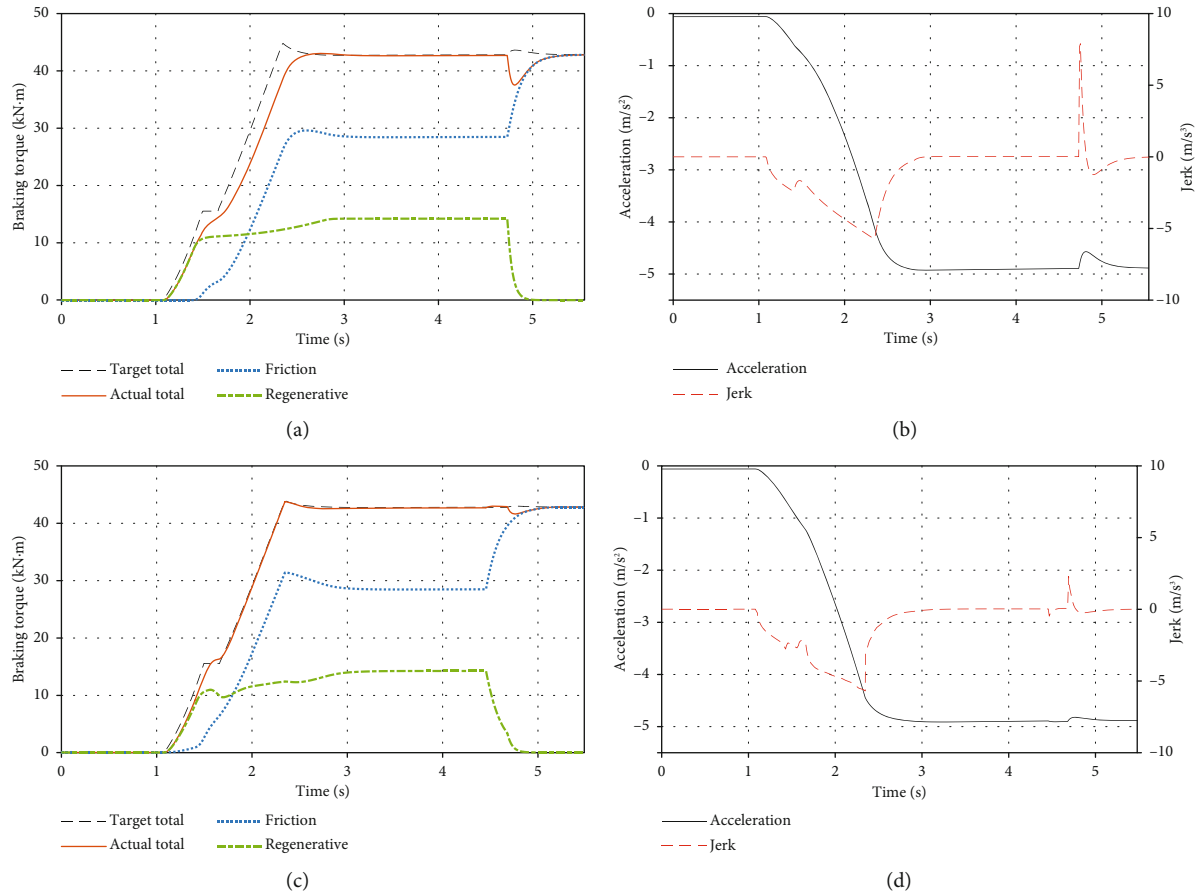

Figure 22: Simulation results under single braking condition 5. (a) Braking torque and (b) acceleration and jerk without coordinated control. (c) Braking torque and (d) acceleration and jerk with coordinated control.

Table 7: Simulation results of single braking conditions.

Single braking condition	Coordinated control	e_1 [a)] (N·m)	e_2 [a)] (N·m)	j_2 [b)] (m/s^3)	Recovered energy (kJ)	Braking distance (m)
Condition 3	Without	—	3231.49	5.025	558.9	68.75
	With	—	91.86	0.12	530.0	68.39
Condition 4	Without	4996.83	5815.04	7.895	877.5	59.86
	With	667.45	554.44	0.850	837.2	59.30
Condition 5	Without	6391.22	6110.58	7.902	864.1	66.63
	With	503.55	1365.21	2.315	821.8	65.75

[a)] e_1 and e_2 denote the maximum torque deviation in transition condition 1 and transition condition 2, respectively; [b)] j_2 denotes the maximum jerk in transition condition 2.

Table 5 shows the simulation results of braking performance in different torque distribution strategies and load states under two single braking conditions. Among them, the energy recovery rate ξ is defined as follows:

$$\xi = \frac{E_{reg}}{E_b} = \frac{\int U_{bat} I_{bat} \mathrm{d}t}{1/2 m v_0^2}, \tag{32}$$

where E_{reg} is the recovered braking energy and E_b is the total energy dissipated in the whole braking process, that is, the kinetic energy of the BET at the initial moment.

The following findings can be drawn: in terms of braking time and braking distance, the proposed strategy outperforms the two benchmark strategies under any braking intensity and load state, showing better braking safety. In terms of braking energy recovery, the proposed strategy achieves the best performance at low braking intensity, and strategy A has a similar or even better effect at high braking intensity, due to its longer braking time. On the whole, the proposed torque distribution strategy has better comprehensive braking performance.

5.1.4. CHTC-D Condition. CHTC-D (China heavy-duty commercial vehicle test cycle-dump) is developed for the

testing and evaluation of energy consumption and emissions of dump trucks, which is used to compare the energy-saving effect of three torque distribution strategies. The classic two-parameter shift schedule was adopted during the driving process, and the vehicle speed can be followed well in various states, as shown in Figure 17.

Figure 18 shows the simulation results in three load states under CHTC-D condition, and the initial battery SOC of the BET is set as 80%. It can be observed that strategy C has a much larger percentage of regenerative braking, and its final SOC is significantly higher than the other two strategies. In addition, the recovered braking energy and energy recovery rate of the three torque distribution strategies during the entire process are compared in Figure 19. The recovered energy increases in proportion to the load mass, but the energy recovery rate does not show a direct correlation with the load mass. The energy recovery rate of strategy C reaches more than 40% in any load state, which greatly improves the energy efficiency of the BETs.

5.2. Simulation and Analysis of Coordinated Control Strategy. To verify the effectiveness of the proposed coordinated control strategy in the two common braking mode transition conditions, three single braking conditions with different initial speeds and braking intensities were designed as shown in Table 6. The BET runs at the set initial speed and starts braking at 1 s. The braking intensity gradually increases to the target value and remains until the vehicle speed drops to 0.

Figures 20–22 show the simulation results with and without coordinated control in the loaded state. Due to the small braking intensity in single braking condition 3, regenerative braking can meet the torque demand of the drive axle, so there is no transition condition 1. Without coordinated control, the maximum torque deviation and the maximum jerk in transition condition 2 reach 3231.49 N·m and 5.025 m/s^3, respectively. With coordinated control, the EMB system starts to intervene before the speed drops to the low-speed threshold, and the motor regenerative braking is used to compensate for the hysteresis of friction braking, which almost eliminates the torque deviation during the braking mode switching process so that the vehicle can decelerate smoothly.

Under single braking condition 4, without coordinated control, the friction braking begins to participate when the regenerative braking torque increases to the maximum. At this time, the motor is operating in a saturated state and no longer can compensate for torque deviation. With coordinated control, due to the correction of regenerative braking torque, the motor outputs relatively large torque during the increasing braking intensity, reserving space to compensate for friction braking torque deviation, so that the actual total torque can follow the target well in transition condition 1, as shown in Figure 21(c). In contrast, the braking intensity and vehicle speed of single braking condition 5 are higher, so larger torque compensation space needs to be reserved, and the EMB system participates earlier, as shown in Figure 22(c). When the braking intensity is no longer increased, the motor outputs the maximum regenerative braking torque to ensure energy recovery efficiency. Comparing Figures 21 and 22 shows that the different braking intensities in single braking conditions result in the difference in the advance degree of regenerative braking withdrawal in transition condition 2. With coordinated control, the difference between the actual torque and the target torque is significantly reduced, and the fluctuation of acceleration is effectively suppressed, which greatly improves the braking comfort.

By analyzing the influence of coordinated control on braking energy recovery, it can be observed from Table 7 that the loss of braking energy recovery is less because the single braking condition 3 has no transition condition 1 and the braking intensity and speed are low. To enable the motor to obtain the torque compensation ability, the energy recovered in the whole braking process is reduced by 40.3 kJ and 42.3 kJ, respectively, under single braking conditions 4 and 5.

In general, the proposed coordinated control strategy solves the problem of response lag and torque deficit in the two common braking mode transition conditions at the expense of slight braking energy, and the braking distance is shortened with the consideration of the composite braking coordination and energy recovery efficiency.

6. Conclusion

In this study, the four-axle BET equipped with an EMB system was taken as the research object, and its composite braking control strategy was presented, including torque distribution strategy and dynamic coordination control strategy. The segmented torque distribution strategy maximizes braking energy recovery while meeting ECE regulations even in the presence of the sensor or control error. This strategy showed better comprehensive performance than the other two benchmark strategies, with the energy recovery rate of 44.58%, 46.07%, and 40.68% in the unloaded, loaded, and overloaded states, respectively, under CHTC-D condition, which effectively improves the energy utilization efficiency and the driving range of BETs.

The coordinated control strategy based on regenerative braking torque compensation was proposed to solve the uncoordinated problem caused by the different response characteristics of the braking subsystems in the two common braking mode transition conditions. The regenerative braking torque was corrected based on fuzzy logic in transition condition 1, and the timing of braking mode switching was advanced according to the real-time braking intensity in transition condition 2, so that the motor can output braking torque sufficient to compensate for torque deviations caused by the hysteresis of the EMB system. An adjustment factor was introduced into the regenerative braking torque control to eliminate the torque fluctuation when the two braking torques change in reverse. The simulation results showed that the coordinated control strategy reduces the difference between actual torque and target torque to less than 1.4 kN·m at the expense of losing a small amount of braking energy, which improves the vehicle riding comfort and shortens the braking distance.

The proposed control strategy has satisfactory performance and low complexity, which is suitable for practical application. In the subsequent research, it will be further verified by the hardware-in-the-loop simulation and real

vehicle test. Moreover, the composite braking control strategy for BETs under downhill conditions needs to be studied deeply. Downhill safety has always been a vital issue, and the tradeoff between braking energy recovery and battery loss should be considered in this case.

Data Availability

No underlying data was collected or produced in this study.

Conflicts of Interest

The authors declare that there is no conflict of interest.

Acknowledgments

This work was supported in part by the National Natural Science Foundation of China (52172362), in part by the Major Science and Technology Projects of Shaanxi Province (2020ZDZX06-01-01), in part by the Fok Yingdong Young Teachers Fund Project (171103), and in part by the Key Research and Development Program of Shaanxi (2020ZDLGY16-01, 2020ZDLGY16-02, and 2021ZDLGY12-01).

References

[1] X. Z. Zhang, Z. H. Lin, C. Crawford, and S. X. Li, "Techno-economic comparison of electrification for heavy-duty trucks in China by 2040," *Transportation Research Part D: Transport and Environment*, vol. 102, article 103152, 2022.

[2] M. A. Bhuiyan, Q. N. Zhang, V. Khare, A. Mikhaylov, G. Pinter, and X. W. Huang, "Renewable energy consumption and economic growth nexus-a systematic literature review," *Frontiers in Environmental Science*, vol. 10, article 878394, 2022.

[3] S. M. Lajevardi, J. Axsen, and C. Crawford, "Simulating competition among heavy-duty zero-emissions vehicles under different infrastructure conditions," *Transportation Research Part D: Transport and Environment*, vol. 106, article 103254, 2022.

[4] S. LaMonaca and L. Ryan, "The state of play in electric vehicle charging services - a review of infrastructure provision, players, and policies," *Renewable and Sustainable Energy Reviews*, vol. 154, p. 111733, 2022.

[5] B. Nykvist and O. Olsson, "The feasibility of heavy battery electric trucks," *Joule*, vol. 5, no. 4, pp. 901–913, 2021.

[6] W. F. Li, H. P. Du, and W. H. Li, "Four-wheel electric braking system configuration with new braking torque distribution strategy for improving energy recovery efficiency," *IEEE Transactions on Intelligent Transportation Systems*, vol. 21, no. 1, pp. 87–103, 2020.

[7] J. G. Ruan, P. D. Walker, P. A. Watterson, and N. Zhang, "The dynamic performance and economic benefit of a blended braking system in a multi-speed battery electric vehicle," *Applied Energy*, vol. 183, pp. 1240–1258, 2016.

[8] D. C. S. Beddows and R. M. Harrison, "PM10 and PM2.5 emission factors for non-exhaust particles from road vehicles: dependence upon vehicle mass and implications for battery electric vehicles," *Atmospheric Environment*, vol. 244, article 117886, 2021.

[9] S. Q. Li, B. Yu, and X. Y. Feng, "Research on braking energy recovery strategy of electric vehicle based on ECE regulation and I curve," *Science Progress*, vol. 103, no. 1, article 36850419877762, 2020.

[10] P. Spichartz and C. Sourkounis, "Brake force distributions optimised with regard to energy recovery for electric vehicles with single front-wheel drive or rear-wheel drive," *IET Electrical Systems in Transportation*, vol. 9, no. 4, pp. 186–195, 2019.

[11] J. Z. Zhang, C. Lv, M. Z. Qiu, Y. T. Li, and D. S. Sun, "Braking energy regeneration control of a fuel cell hybrid electric bus," *Energy conversion and management*, vol. 76, pp. 1117–1124, 2013.

[12] C. S. N. Kumar and S. C. Subramanian, "Cooperative control of regenerative braking and friction braking for a hybrid electric vehicle," *Proceedings of the Institution of Mechanical Engineers, Part D: Journal of Automobile Engineering*, vol. 230, no. 1, pp. 103–116, 2016.

[13] J. Z. Zhang, C. Lv, J. F. Gou, and D. C. Kong, "Cooperative control of regenerative braking and hydraulic braking of an electrified passenger car," *Proceedings of the Institution of Mechanical Engineers, Part D: Journal of Automobile Engineering*, vol. 226, no. 10, pp. 1289–1302, 2012.

[14] S. W. Xu, X. Zhao, N. X. Yang, and Z. F. Bai, "Control strategy of braking energy recovery for range-extended electric commercial vehicles by considering braking intention recognition and electropneumatic braking compensation," *Energy Technology*, vol. 8, no. 9, article 2000407, 2020.

[15] M. A. Bhuiyan, H. Dincer, S. Yuksel et al., "Economic indicators and bioenergy supply in developed economies: QROF-DEMATEL and random forest models," *Energy Reports*, vol. 8, pp. 561–570, 2022.

[16] J. Z. Li, S. Yuksel, H. Dincer, A. Mikhaylov, and S. E. Barykin, "Bipolar q-ROF hybrid decision making model with golden cut for analyzing the levelized cost of renewable energy alternatives," *IEEE Access*, vol. 10, pp. 42507–42517, 2022.

[17] H. Dincer, S. Yuksel, A. Mikhaylov, S. E. Barykin, T. Aksoy, and U. Hacioglu, "Analysis of environmental priorities for green project investments using an integrated q-rung orthopair fuzzy modeling," *IEEE Access*, vol. 10, pp. 50996–51007, 2022.

[18] G. Q. Xu, W. M. Li, K. Xu, and Z. B. Song, "An intelligent regenerative braking strategy for electric vehicles," *Energies*, vol. 4, no. 9, pp. 1461–1477, 2011.

[19] Z. J. Zhang and Y. Y. Dong, "Safety ensurence research on the regenerative braking system of electric vehicle," *International Journal of Pattern Recognition and Artificial Intelligence*, vol. 33, no. 4, p. 1959014, 2019.

[20] J. Y. Huang, D. T. Qin, and Z. Y. Peng, "Effect of energy-regenerative braking on electric vehicle battery thermal management and control method based on simulation investigation," *Energy Conversion and Management*, vol. 105, pp. 1157–1165, 2015.

[21] W. Xu, H. Chen, H. Y. Zhao, and B. T. Ren, "Torque optimization control for electric vehicles with four in-wheel motors equipped with regenerative braking system," *Mechatronics*, vol. 57, pp. 95–108, 2019.

[22] D. Paul, E. Velenis, D. P. Cao, and T. Dobo, "Optimal mu-estimation-based regenerative braking strategy for an AWD HEV," *IEEE Transactions on Transportation Electrification*, vol. 3, no. 1, pp. 249–258, 2017.

[23] F. C. Sun, W. Liu, H. W. He, and H. Q. Guo, "An integrated control strategy for the composite braking system of an electric vehicle with independently driven axles," *Vehicle System Dynamics*, vol. 54, no. 8, pp. 1031–1052, 2016.

[24] C. Y. Wang, W. Z. Zhao, and W. K. Li, "Braking sense consistency strategy of electro-hydraulic composite braking system," *Mechanical Systems and Signal Processing*, vol. 109, pp. 196–219, 2018.

[25] N. L. Feng, J. W. Yong, and Z. Q. Zhan, "A direct multiple shooting method to improve vehicle handling and stability for four hub-wheel-drive electric vehicle during regenerative braking," *Transactions of the British Orthopaedic Society*, vol. 234, no. 4, pp. 1047–1056, 2020.

[26] H. Q. Guo, H. W. He, and X. L. Xiao, "A predictive distribution model for cooperative braking system of an electric vehicle," *Mathematical Problems in Engineering*, vol. 2014, Article ID 828269, 11 pages, 2014.

[27] H. Z. Sun, H. Wang, and X. C. Zhao, "Line braking torque allocation scheme for minimal braking loss of four-wheel-drive electric vehicles," *IEEE Transactions on Vehicular Technology*, vol. 68, no. 1, pp. 180–192, 2019.

[28] A. Pennycott, L. De Novellis, P. Gruber, and A. Sorniotti, "Optimal braking force allocation for a four-wheel drive fully electric vehicle," *Proceedings of the Institution of Mechanical Engineers, Part I: Journal of Systems and Control Engineering*, vol. 228, no. 8, pp. 621–628, 2014.

[29] F. Naseri, E. Farjah, and T. Ghanbari, "An efficient regenerative braking system based on battery/supercapacitor for electric, hybrid, and plug-in hybrid electric vehicles with BLDC motor," *IEEE Transactions on Vehicular Technology*, vol. 66, p. 3724, 2016.

[30] M. L. Shang, L. A. Chu, J. H. Guo, Y. Fang, and F. K. Zhou, *Braking Force Dynamic Coordinated Control for Hybrid Electric Vehicles, 2nd IEEE International Conference on Advanced Computer Control*, IEEE, Shenyang, 2010.

[31] M. H. Kwon, J. H. Park, G. S. Gwak, J. W. Huh, H. K. Choi, and S. H. Hwang, "Cooperative control for friction and regenerative braking systems considering dynamic characteristic and temperature condition," *International Journal of Automotive Technology*, vol. 17, no. 3, pp. 437–446, 2016.

[32] Q. He, Y. Yang, C. Luo, J. Zhai, R. H. Luo, and C. Y. Fu, "Energy recovery strategy optimization of dual-motor drive electric vehicle based on braking safety and efficient recovery," *Energy*, vol. 248, p. 123543, 2022.

[33] E. Cabukoglu, G. Georges, L. Kung, G. Pareschi, and K. Boulouchos, "Battery electric propulsion: an option for heavy-duty vehicles? Results from a Swiss case-study," *Transportation Research Part C: Emerging Technologies*, vol. 88, pp. 107–123, 2018.

[34] V. A. Bogomolov, V. I. Klimenko, D. N. Leontiev, S. V. Ponikarovska, A. A. Kashkanov, and V. Y. Kucheruk, "Plotting the adhesion utilization curves for multi-axle vehicles," *B UNIV KARAGANDA-PHY*, vol. 101, no. 1, pp. 35–45, 2021.

[35] J. J. Zhang, Y. Yang, M. H. Hu, Z. Yang, and C. Y. Fu, "Longitudinal-vertical comprehensive control for four-wheel drive pure electric vehicle considering energy recovery and ride comfort," *Energy*, vol. 236, p. 121417, 2021.

[36] H. J. Wang, S. H. Yuan, and J. S. Xu, *Research on Braking Strategy and Performance Considering the Tire Model for Multi-Axle Vehicle*, IEEE Transportation Electrification Conference and Expo, IEEE, Beijing, 2014.

[37] L. Wang, J. Ma, X. Zhao, X. B. Li, K. Zhang, and Z. P. Jiao, "Adaptive robust unscented Kalman filter-based state-of-charge estimation for lithium-ion batteries with multi-parameter updating," *Electrochimica Acta*, vol. 426, p. 140760, 2022.

[38] L. Li, X. Y. Wang, R. Xiong, K. He, and X. J. Li, "AMT downshifting strategy design of HEV during regenerative braking process for energy conservation," *Applied Energy*, vol. 183, pp. 914–925, 2016.

[39] S. Heydari, P. Fajri, R. Sabzehgar, and A. Asrari, "Optimal brake allocation in electric vehicles for maximizing energy harvesting during braking," *IEEE Transactions on Energy Conversion*, vol. 35, no. 4, pp. 1806–1814, 2020.